Journal of Materials Chemistry C

ROYAL SOCIETY OF CHEMISTRY

PAPER

View Article Online
View Journal | View Issue

Cite this: J. Mater. Chem. C, 2024, 12, 11051

Advanced lead-free double perovskites/silica hybrid nanocrystals for highly stable light-emitting diodes†

Jindou Shi, [a] Zeyu Wang,*[b] Luxia Xu,[c] Junnan Wang,[a] Zheyuan Da,[a] Chen Zhang,[a] Yongqiang Ji, [a] Qing Yao, [a] Youlong Xu, [a] Nikolai V. Gaponenko,[d] Jinshou Tian[c] and Minqiang Wang[a]

Received 13th February 2024,
Accepted 15th May 2024

DOI: 10.1039/d4tc00585f

rsc.li/materials-c

The commercial viability of fluorescent materials is critically contingent on their thermal stability. Recent interest has converged on lead-free double perovskites (DPs), renowned for their optical properties mirroring those of traditional lead-based counterparts and superior atmospheric stability. However, these materials encounter significant fluorescence degradation in thermal environments, a challenging scenario given the high temperatures endemic to the surfaces of optoelectronic devices during prolonged operation, detrimentally impacting the fluorescent attributes of lead-free DPs. To address this challenge, *in situ* synthesis of lead-free DP nanocrystals (NCs) within KIT-6 mesoporous molecular sieves is proposed, yielding $Cs_2AgIn_{0.98}Bi_{0.02}Cl_6$@KIT-6 NCs with enhanced optical qualities. Experimental results demonstrate a marked enhancement in the fluorescence thermal stability of these NCs, attributed to the protective KIT-6 shell layer. Subjected to high power operation (100 mA) for 270 minutes, the fabricated orange light-emitting diode (LED) device maintained 80% of initial luminous efficiency, despite the resultant elevated surface temperature of 326.8 K. Therefore, this novel *in situ* assembly approach significantly bolsters the operational stability of lead-free DPs, paving the way for their potential commercial applications.

Introduction

Recent advancements have positioned lead-free double perovskite (DP) nanocrystals (NCs) as a promising alternative to conventional lead halide perovskite NCs, offering reduced toxicity and enhanced stability under atmospheric conditions.[1–6] Applications of these materials have extended across various domains, notably in solar cells and photodetectors.[7–12] Concurrently, the enhancement of the optical properties of lead-free DP materials through ion doping has emerged as a focal point of research,[13–15] setting a foundational platform for their integration into light-emitting diodes (LEDs).[16–19] However, a critical challenge is the high temperatures generated on optoelectronic device surfaces during extended operation, adversely affecting the optical performance of fluorescent materials, including lead-free DPs.[20–22] To address this challenge, a comprehensive study for enhancing the fluorescence thermal stability of lead-free DP materials becomes imperative for their potential commercial deployment.

Recent studies have delved into the thermal stability of lead-free DP materials.[23–25] For instance, $Cs_2AgInCl_6$ powder exhibited a significant weight loss at 200 °C,[26] while $Cs_2NaBiCl_6$-based UV detectors demonstrated long-term operational stability at 333 K.[11] Furthermore, $Cs_2Ag_{0.7}Na_{0.3}InCl_6$:Bi microcrystals (MCs), when subjected to 398 K for 500 hours, retained nearly 86% of the initial photoluminescence (PL) intensity.[27] Concurrently, various strategies to enhance thermal stability have been explored, including employing Cu^{2+} doping to maintain the stability of $Cs_2SbAgCl_6$ MCs at 110 °C.[28] Despite these advancements, comprehensive strategies for enhancing the stability of lead-free DP materials, particularly for their optical applications in nanocrystals (NCs), remain limited. Therefore, addressing the challenges posed by external thermal environments is crucial for the advancement of lead-free DP NCs in optical applications.

In this study, a robust KIT-6 mesoporous molecular sieve was utilized as a protective surface shell layer. An *in situ*

[a] Electronic Materials Research Laboratory, Key Laboratory of the Ministry of Education International Center for Dielectric Research&Shannxi Engineering Research Center of Advanced Energy Materials and Devices, Xi'an Jiaotong University, 710049 Xi'an, China
[b] Frontier Institute of Science and Technology (FIST), and Micro- and Nano-technology Research Center of State Key Laboratory for Manufacturing Systems Engineering, Xi'an Jiaotong University, 710049, Xi'an, China. E-mail: zeyu.wang@xjtu.edu.cn
[c] Xi'an Institute of Optics and Precision Mechanics, Xi'an, 710119, Shaanxi, P. R. China
[d] Belarusian State University of Informatics and Radioelectronics, P. Browki 6, 220013, Minsk, Belarus

† Electronic supplementary information (ESI) available. See DOI: https://doi.org/10.1039/d4tc00585f

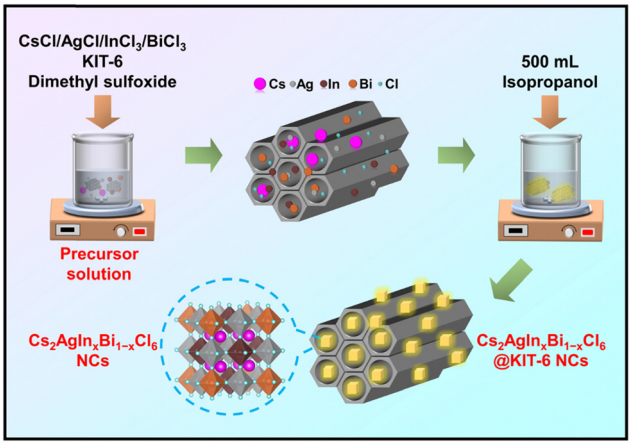

Fig. 1 Schematic illustration of $Cs_2AgIn_xBi_{1-x}Cl_6$@KIT-6 NCs with different In^{3+} contents fabricated using the *in situ* assembling method.

self-assembly process was developed for growing $Cs_2AgInCl_6$ NCs within internal pores of KIT-6, resulting in the formation of highly stable $Cs_2AgInCl_6$@KIT-6 NCs. Optical absorption enhancement was then achieved through *in situ* Bi^{3+} doping, leading to the emission of bright orange light from $Cs_2AgIn_{0.98}Bi_{0.02}Cl_6$@KIT-6 NCs (Fig. 1). A comparative analysis of the fluorescence stability was conducted between$Cs_2AgIn_{0.98}Bi_{0.02}Cl_6$ NCs without shell layer protection and $Cs_2AgIn_{0.98}Bi_{0.02}Cl_6$@KIT-6 NCs with the shell layer in a high temperature environment. This analysis included an in-depth exploration of the fluorescence quenching mechanism and revealed that the $Cs_2AgIn_{0.98}Bi_{0.02}Cl_6$@KIT-6 NCs exhibited markedly improved fluorescence thermal stability, attributed to the effective thermal isolation provided by the KIT-6 shell layer. In a practical application, two LEDs were assembled using $Cs_2AgIn_{0.98}Bi_{0.02}Cl_6$ NCs and $Cs_2AgIn_{0.98}Bi_{0.02}Cl_6$@KIT-6 NCs, respectively. The optoelectronic parameters and surface temperatures of these devices were monitored during high-power, long-duration operation. After 270 minutes of continuous operation, the LED comprising $Cs_2AgIn_{0.98}Bi_{0.02}Cl_6$@KIT-6 NCs retained 80% of its initial luminous efficiency, significantly outperforming the LED with $Cs_2AgIn_{0.98}Bi_{0.02}Cl_6$ NCs, which maintained only 26% of efficiency at a similar surface temperature of 326.8 K. This substantial enhancement in the fluorescence thermal stability of $Cs_2AgIn_{0.98}Bi_{0.02}Cl_6$@KIT-6 NCs, afforded by KIT-6 coating, is poised to significantly contribute to the development of optoelectronic devices and expedite the commercialization of lead-free DP materials.

Results and discussion

The $Cs_2AgIn_xBi_{1-x}Cl_6$@KIT-6 NCs with different In^{3+} contents were synthesized using an *in situ* assembly method. Subsequently, the structure and microscopic morphology of $Cs_2AgIn_xBi_{1-x}Cl_6$@KIT-6 NCs with different In^{3+} contents were investigated with assistance from X-ray diffraction (XRD) and transmission electron microscopy (TEM). In order to obtain the actual doping ratio of In^{3+}, the elements in $Cs_2AgIn_xBi_{1-x}Cl_6$@KIT-6 NCs were quantitatively analyzed by inductively coupled plasma emission spectrometry (ICP-OES) (Table S1). The XRD patterns of $Cs_2AgIn_xBi_{1-x}Cl_6$@KIT-6 NCs with different In^{3+} contents indicated that distinct highly crystalline DP diffraction peaks were detected in all the samples, which corresponded perfectly to the pure bulk $Cs_2AgInCl_6$ (ICSD: 257115) at the bottom (Fig. 2a). Moreover, the XRD patterns of $Cs_2AgIn_xBi_{1-x}Cl_6$@KIT-6 NCs with different In^{3+} contents all presented a broad diffraction peak at 20°, originating from the amorphous KIT-6 mesoporous molecular sieve (Fig. S1, ESI†),

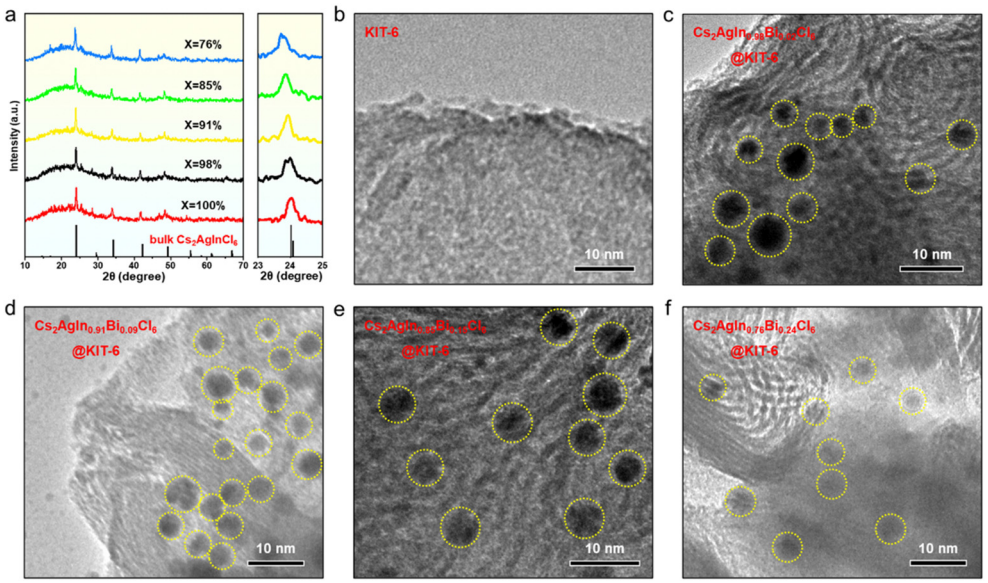

Fig. 2 (a) XRD patterns of $Cs_2AgIn_xBi_{1-x}Cl_6$@KIT-6 NCs with different In^{3+} contents (the bottom corresponds to a pure bulk $Cs_2AgInCl_6$ (ICSD: 257115)). Magnification of the XRD patterns is in the 23°–25° range. TEM images of (b) KIT-6 mesoporous molecular sieves, (c) $Cs_2AgIn_{0.98}Bi_{0.02}Cl_6$@KIT-6 NCs, (d) $Cs_2AgIn_{0.91}Bi_{0.09}Cl_6$@KIT-6 NCs, (d) $Cs_2AgIn_{0.85}Bi_{0.15}Cl_6$@KIT-6 NCs and (f) $Cs_2AgIn_{0.76}Bi_{0.24}Cl_6$@KIT-6 NCs.

which indicated that the compositing of $Cs_2AgIn_xBi_{1-x}Cl_6$ with the KIT-6 molecular sieve could be achieved using the *in situ* assembly method. Meanwhile, the magnified XRD patterns of $Cs_2AgIn_xBi_{1-x}Cl_6$@KIT-6 NCs with different In^{3+} contents in the 23°–25° range displayed that the diffraction peaks shifted to a lower 2θ angle with the reduced In^{3+} content (Fig. 2a), resulting from the fact that the ionic radius of Bi^{3+} is larger (117 pm), which caused the lattice expansion after substituting the smaller ionic radius of In^{3+} (94 pm), a similar phenomenon reported in the previous synthesis of other lead-free DP materials.[29,30] The microscopic morphology of different samples was further observed, and the TEM image of the pure KIT-6 mesoporous molecular sieve showed that no other crystalline phases existed within it (Fig. 2b). However, $Cs_2AgIn_xBi_{1-x}Cl_6$@KIT-6 NCs obtained by *in situ* assembly not only had the KIT-6 shell layer, but also had some NCs inside it (yellow circles), whose average size was maintained within 5 nm because of the confined growth of mesoporous channels in KIT-6 (Fig. 2c–f and Fig. S2a–d, ESI†). Furthermore, the elemental mapping spectra of $Cs_2AgIn_xBi_{1-x}Cl_6$@KIT-6 NCs showed that the NCs in the KIT-6 mesoporous molecular sieve belonged to $Cs_2AgIn_xBi_{1-x}Cl_6$ (Fig. S3a and b, ESI†), indicating that $Cs_2AgIn_xBi_{1-x}Cl_6$ NCs had completed confined growth in the mesoporous channels of KIT-6 at this time. Subsequently, the surface pore structure of the KIT-6 mesoporous molecular sieve was investigated by using Brunauer–Emmett–Teller (BET) nitrogen adsorption–desorption isotherms, and a typical type IV adsorption isotherm with a sharp capillary coalescence step and a H1-type hysteresis loop appeared under higher relative pressures.[31–33] Monolayer adsorption and multilayer adsorption were observed sequentially as the relative pressure increased. The adsorption isotherm steepened when capillary condensation occurred under pressure, and surface adsorption eventually occurred. Due to these, the adsorption capacity increased slowly in the range of relative pressures (p/p_0) between 0.2 and 0.5, indicating the existence of mesopores. The KIT-6 adsorption capacity increased rapidly as the relative pressure elevated to 0.55–0.89, accompanied by an obvious H1-type hysteresis loop, which is a typical mesoporous capillary condensation phenomenon, indicating that it had a regular pore size distribution and a uniform mesoporous structure. Furthermore, the increasing trend of the adsorption capacity gradually slowed down as the relative pressure continued to be elevated, and the adsorption gradually reached saturation at this time (Fig. S4a and b, ESI†). Table S2 (ESI†) presents the structural data of KIT-6 mesoporous molecular sieves measured using the Barrett–Joyner–Halenda method. It can be seen that the specific surface area of pure KIT-6 was ≈813.13 $m^2\ g^{-1}$ with a pore width of ≈7.06 nm (Fig. S4c, ESI†). However, the specific surface area of $Cs_2AgIn_{0.98}Bi_{0.02}Cl_6$@KIT-6 decreased to 550.59 $m^2\ g^{-1}$ and the pore volume also decreased from 1.3588 $cm^3\ g^{-1}$ to 1.0001 $cm^3\ g^{-1}$, implying that $Cs_2AgIn_{0.98}Bi_{0.02}Cl_6$ had filled into the mesopores of KIT-6. Meanwhile, the pore size of $Cs_2AgIn_{0.98}Bi_{0.02}Cl_6$@KIT-6 still maintained a similar value to that of KIT-6 (≈6.98 nm) (Fig. S4d, ESI†), which revealed that KIT-6 molecular sieves sustained a stable void structure during the *in situ* assembly process. Combining the above characterization results, the confined growth of $Cs_2AgIn_xBi_{1-x}Cl_6$ NCs with different In^{3+} contents in KIT-6 mesoporous molecular sieves can be achieved by using this convenient *in situ* assembly method, thereby obtaining high-quality $Cs_2AgIn_xBi_{1-x}Cl_6$@KIT-6 core–shell NCs.

In particular, the optical properties of $Cs_2AgIn_xBi_{1-x}Cl_6$@KIT-6 NCs with different In^{3+} contents were explored in depth, thereby effectively enhancing the competitiveness of lead-free DP materials in the future optical lighting markets. Firstly, the UV-vis reflectance spectrum data (Fig. S5, ESI†) of $Cs_2AgIn_xBi_{1-x}Cl_6$@KIT-6 NCs with different In^{3+} contents were converted to pseudo-absorbance (Fig. 3a) using the Kubelka–Munk (KM) function, $\alpha = (1-R)^2/2R$, where α is the optical absorption coefficient and R is the reflectance.[34] Obviously, no exciton absorption peaks were observed in the absorbance spectrum of $Cs_2AgInCl_6$@KIT-6 NCs (Fig. 3a), exhibiting a weak optical absorption coefficient around the bandgap, which is consistent with the previously reported properties of pure $Cs_2AgInCl_6$ NCs, implying that it was unable to absorb enough energy for complete optical emission.[35,36] Undoubtedly, the PL spectrum corresponding to $Cs_2AgInCl_6$@KIT-6 NCs also did not show significant fluorescence emission peaks (Fig. 3b), further confirming the unsuitability of $Cs_2AgInCl_6$@KIT-6 NCs for optoelectronic applications. In contrast, $Cs_2AgIn_xBi_{1-x}Cl_6$@KIT-6 NCs (x = 76%, 85%, 91%, and 98%) showed an exciton absorption peak at 370 nm after doping with Bi^{3+} (Fig. 3a), originating from the s → p orbital leaps of Bi^{3+}, which mainly consisted of dipole-allowed transition $^1S_0 \rightarrow {}^1P_1$, spin–orbital-allowed transition $^1S_0 \rightarrow {}^3P_1$, and forbidden

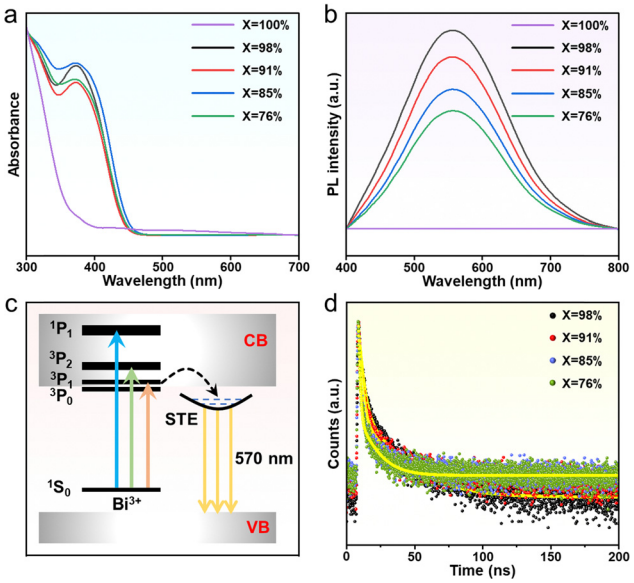

Fig. 3 (a) Absorbance and (b) PL spectra of $Cs_2AgIn_xBi_{1-x}Cl_6$@KIT-6 NCs with different In^{3+} contents. (c) Energy-level diagram of $Cs_2AgIn_xBi_{1-x}Cl_6$@KIT-6 NCs and the PL emission mechanism (CB, conduction band; VB, valence band; STE, self-trapped exciton state). (d) Time-resolved PL spectra and fitted curves for $Cs_2AgIn_xBi_{1-x}Cl_6$@KIT-6 NCs with different In^{3+} contents.

transition $^1S_0 \rightarrow {}^3P_2$ (Fig. 3c).[34] Subsequently, under 365 nm UV excitation, $Cs_2AgIn_xBi_{1-x}Cl_6$@KIT-6 NCs (x = 76%, 85%, 91%, and 98%) exhibited a broad PL emission peak at 570 nm (Fig. 3b), which benefited from the breaking of the forbidden transition of Bi^{3+} induced by In^{3+} in the host, enabling enhanced absorption of the transition, ensuring that large amounts of energy were efficiently transferred to the self-trapping exciton (STE) state, thereby emitting a bright orange light (Fig. 3c).[17,36] Interestingly, the corresponding PL intensity decayed when the Bi^{3+} doping content gradually increased (Fig. 3b). For a deeper understanding of the luminescence mechanism, crystal models of pure-phase $Cs_2AgInCl_6$, slightly doped $Cs_2AgIn_{0.75}Bi_{0.25}Cl_6$, and over-doped $Cs_2AgIn_{0.5}Bi_{0.5}Cl_6$ were constructed (Fig. 4a–c), and their electronic structures were calculated by using Perdew–Burke–Ernzerhof (PBE)-DFT calculations, respectively (Fig. 4d–f). $Cs_2AgInCl_6$ exhibited a direct band gap, and its valence band maximum (VBM) and conduction band minimum (CBM) were simultaneously located at the G point (Fig. 4d). The VBM of $Cs_2AgInCl_6$ consisted of In-p, Cl-p, and Ag-d orbitals, while the CBM consisted of Ag-s, Cl-p, and In-s orbitals (Fig. S6a, ESI†). Unfortunately, the optical transition between the band edge states at the G point was parity forbidden, which was extremely weak, resulting in its inability to absorb enough energy for supporting fluorescence emission, and similar findings have been reported in previous studies.[37,38] With a small amount of Bi^{3+} doping, $Cs_2AgIn_{0.75}Bi_{0.25}Cl_6$ also displayed a direct band gap (Fig. 4e), where the VBM consisted of Cl-p, Ag-d, In-p, and Bi-s orbitals, while the minimum conduction band consisted of Cl-p, In-s, Bi-p, and Ag-s orbitals (Fig. S6b, ESI†). Optical transition of $Cs_2AgIn_{0.75}Bi_{0.25}Cl_6$ at the G-point was also forbidden, but the s → p direct transition introduced by high-energy Bi^{3+} doping was able to break this parity forbidden prompting an enhanced absorption, allowing relaxation of electrons and holes under forbidden photoexcitation, resulting in orange light emission. However, after the content of Bi^{3+} was further increased, $Cs_2AgIn_{0.5}Bi_{0.5}Cl_6$ showed an indirect band gap from the Q-point to the G-point (Fig. 4f), where the VBM consisted of Cl-p, Ag-d, In-p, and Bi-s orbitals, while the CBM consisted of Cl-p, In-s, Bi-p, and Ag-s orbitals (Fig. S6c, ESI†). Although the orbital composition of $Cs_2AgIn_{0.5}Bi_{0.5}Cl_6$ was consistent with that of $Cs_2AgIn_{0.75}Bi_{0.25}Cl_6$, the excess Bi^{3+} caused the Ag and Bi frontier orbitals in the VBM and the CBM to be mixed, thereby resulting in the Ag–Bi DP crystals displaying an indirect band gap and the fluorescence properties disappear.[36,39] Therefore, the trace Bi^{3+} doping expanded the absorption range of $Cs_2AgIn_xBi_{1-x}Cl_6$@KIT-6 NCs to 450 nm compared to pure $Cs_2AgInCl_6$@KIT-6 NCs, thereby enabling bright orange emission, while excessive doping will decay the fluorescence of $Cs_2AgIn_xBi_{1-x}Cl_6$@KIT-6 NCs (x = 76%, 85%, 91%) (Fig. 3b). Subsequently, the time-resolved PL spectra of the samples were recorded separately for further analysis of the influence of Bi^{3+} doping on the carrier dynamics of $Cs_2AgIn_xBi_{1-x}Cl_6$@KIT-6 NCs (Fig. 3d). The fitting results indicated that the lifetime of $Cs_2AgIn_xBi_{1-x}Cl_6$@KIT-6 NCs decreased from 20.7981 ns to 12.5458 ns with the increased Bi^{3+} content (Table S3, ESI†), which mainly stemmed from the fact that the proportion of the indirect bandgap in the sample was elevated, so that the ratio of radiative recombination was reduced and a similar phenomenon had been found in $Cs_2Ag_xNa_{1-x}BiCl_6$.[16] In summary, the optical properties of $Cs_2AgIn_{0.98}Bi_{0.02}Cl_6$@KIT-6 NCs are the most prominent, which will lay the foundation for their development in the field of optoelectronic devices, and this will be considered as the primary target in the subsequent study.

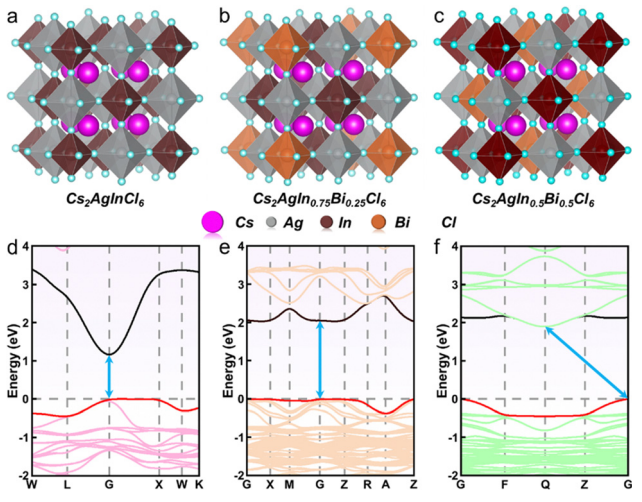

Fig. 4 (a)–(c) Crystal structures of $Cs_2AgIn_xBi_{1-x}Cl_6$ (x = 100%, 75%, and 50%). (d)–(f) Band structures of $Cs_2AgIn_xBi_{1-x}Cl_6$ (x = 100%, 75%, and 50%).

To further understand the enhancement of $Cs_2AgIn_{0.98}Bi_{0.02}Cl_6$ NCs with KIT-6 shell layers, pure $Cs_2AgIn_{0.98}Bi_{0.02}Cl_6$ NCs were obtained using a one-step anti-solvent recrystallisation method. It can be seen that without the confined growth of the mesoporous KIT-6 molecular sieves, the size of pure $Cs_2AgIn_{0.98}Bi_{0.02}Cl_6$ NCs was dramatically larger, with an average particle size of about 50 nm (Fig. 5a and Fig. S7, ESI†). Meanwhile, the elemental mapping spectra of $Cs_2AgIn_{0.98}Bi_{0.02}Cl_6$ NCs showed a uniform distribution of all the elements (Fig. S8, ESI†), confirming the doping into Bi^{3+} in $Cs_2AgInCl_6$ NCs. Moreover, the XRD patterns indicated that no broad peak at 20° belonging to KIT-6 was observed in the pure $Cs_2AgIn_{0.98}Bi_{0.02}Cl_6$ NCs, and the other diffraction peaks all matched exactly with $Cs_2AgIn_{0.98}Bi_{0.02}Cl_6$@KIT-6 NCs, which concluded that pure $Cs_2AgIn_{0.98}Bi_{0.02}Cl_6$ NCs had been obtained at this point (Fig. 5b). On the other hand, compared with the optical properties of $Cs_2AgIn_{0.98}Bi_{0.02}Cl_6$@KIT-6 NCs, the exciton absorption peak of pure $Cs_2AgIn_{0.98}Bi_{0.02}Cl_6$ NCs was particularly pronounced without the surface KIT-6 shell layer, and they were both located at 370 nm (Fig. 5c), which also reflected from another view that KIT-6 does not mask the optical absorption of $Cs_2AgIn_{0.98}Bi_{0.02}Cl_6$ NCs. Differently, the PL emission peak of pure $Cs_2AgIn_{0.98}Bi_{0.02}Cl_6$ NCs appeared weakly red-shifted, which can be attributed to the quantum size effect, as reported in Pb-based perovskite NCs (Fig. 5c).[40] Subsequently, the time-resolved PL spectra of pure $Cs_2AgIn_{0.98}Bi_{0.02}Cl_6$ NCs showed that the lifetime was shorter than that of $Cs_2AgIn_{0.98}Bi_{0.02}Cl_6$@KIT-6 NCs (Fig. 5d), which suggested that their

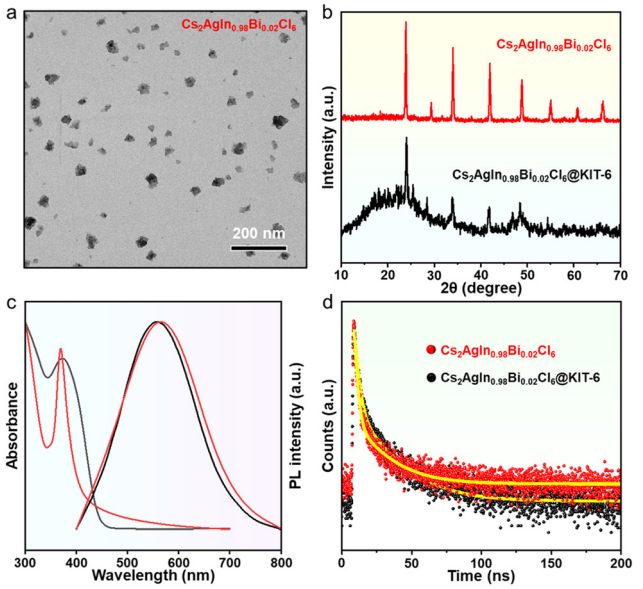

Fig. 5 (a) TEM images of $Cs_2AgIn_{0.98}Bi_{0.02}Cl_6$ NCs. (b) XRD patterns of $Cs_2AgIn_{0.98}Bi_{0.02}Cl_6$ NCs (top) and $Cs_2AgIn_{0.98}Bi_{0.02}Cl_6$@KIT-6 NCs (bottom). (c) Absorbance and PL spectra of $Cs_2AgIn_{0.98}Bi_{0.02}Cl_6$ NCs (red) and $Cs_2AgIn_{0.98}Bi_{0.02}Cl_6$@KIT-6 NCs (black). (d) Time-resolved PL spectra and fitted curves of $Cs_2AgIn_{0.98}Bi_{0.02}Cl_6$ NCs (red dots) and $Cs_2AgIn_{0.98}Bi_{0.02}Cl_6$@KIT-6 NCs (black dots).

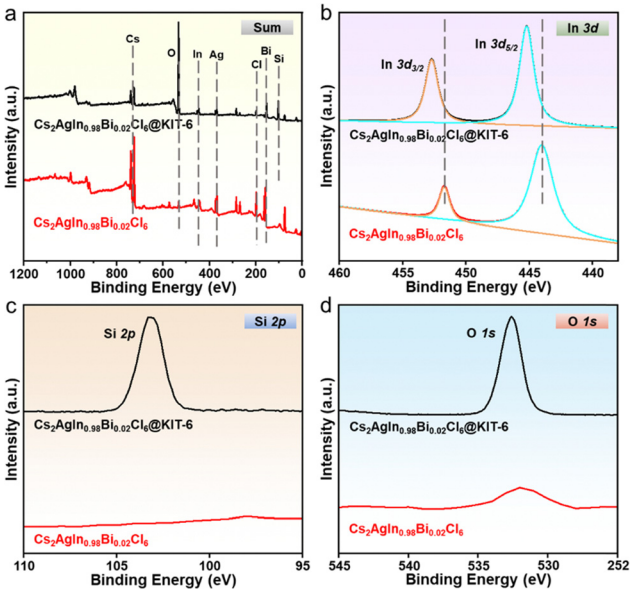

Fig. 6 (a) XPS spectra of $Cs_2AgIn_{0.98}Bi_{0.02}Cl_6$@KIT-6 and $Cs_2AgIn_{0.98}Bi_{0.02}Cl_6$. High-resolution spectra of (b) In 3d, (c) Si 2p, and (d) O 1s.

non-radiative recombination ratio was higher (Table S4, ESI†). This phenomenon can be attributed to the capability of the KIT-6 shell layer to effectively passivate the surface defects of $Cs_2AgIn_{0.98}Bi_{0.02}Cl_6$ NCs, resulting in a higher radiative recombination ratio,[41,42] thereby exhibiting better luminescence efficiency.

Subsequently, the elemental chemical states of $Cs_2AgIn_{0.98}Bi_{0.02}Cl_6$@KIT-6 and $Cs_2AgIn_{0.98}Bi_{0.02}Cl_6$ were compared *via* X-ray photoelectron spectroscopy (XPS), which provided new insights into the combination of $Cs_2AgIn_{0.98}Bi_{0.02}Cl_6$ NCs with KIT-6 mesoporous molecular sieves. Noticeably, the characteristic peaks of Cs, Ag, In, Bi and Cl signals were detected simultaneously in $Cs_2AgIn_{0.98}Bi_{0.02}Cl_6$@KIT-6 and $Cs_2AgIn_{0.98}Bi_{0.02}Cl_6$, which reconfirmed the feasibility of the *in situ* assembly method for the lead-free DP material preparation. Additionally, distinctive Si and O signals, which originated from KIT-6 mesoporous molecular sieves, were detected in $Cs_2AgIn_{0.98}Bi_{0.02}Cl_6$@KIT-6 (Fig. 6a). The high-resolution XPS (HR-XPS) spectra of the In signal in $Cs_2AgIn_{0.98}Bi_{0.02}Cl_6$ were further monitored, and a doublet corresponding to In $3d_{5/2}$ (444.1 eV) and In $3d_{3/2}$ (451.7 eV) was observed clearly due to spin–orbit splitting (Fig. 6b, red). Amusingly, although the In $3d_{5/2}$ and In $3d_{3/2}$ doublets can also be seen in $Cs_2AgIn_{0.98}Bi_{0.02}Cl_6$@KIT-6, their binding energies were elevated to 445.2 eV and 452.8 eV, respectively (Fig. 6b, black). This phenomenon can be attributed to the strong interaction between In^{3+} and the KIT-6 shell layer, and the same phenomenon was observed in the HR-XPS spectra of the other elemental signals (Fig. S9, ESI†). Beyond this, strong characteristic peaks of Si 2p and O1s were detected in $Cs_2AgIn_{0.98}Bi_{0.02}Cl_6$@KIT-6 (Fig. 6c, d, black), while the weaker peak of O1s in $Cs_2AgIn_{0.98}Bi_{0.02}Cl_6$ originated from In-O (Fig. 6 d, red), as also reported in $CsPbBr_3$@ZrO_2 NCs.[43] Combining the enhanced elemental binding energy of the lead-free DP NCs in $Cs_2AgIn_{0.98}Bi_{0.02}Cl_6$@KIT-6, it can be concluded that the binding of the $Cs_2AgIn_{0.98}Bi_{0.02}Cl_6$ NCs and the KIT-6 shell layer should belong to strong chemical bonding rather than simple physical adsorption.[44] Of these, the KIT-6 mesoporous molecular sieves provided better passivation and space-confined growth templates for the $Cs_2AgIn_{0.98}Bi_{0.02}Cl_6$ NCs, so that $Cs_2AgIn_{0.98}Bi_{0.02}Cl_6$@KIT-6 NCs should possess superior PL properties and enhanced stability.

In practical illumination applications, fluorescent materials inevitably suffer from the disturbance created by the thermal environment on the surface of the device, which will place more strict demands on their optical stability. Here, the fluorescence thermal stability of $Cs_2AgIn_{0.98}Bi_{0.02}Cl_6$ NCs and $Cs_2AgIn_{0.98}Bi_{0.02}Cl_6$@KIT-6 NCs was assessed by heating–cooling cycles at high temperatures, and the variation of the PL spectra of the samples with the temperature increased at 373 K was observed, respectively (Fig. 7a and e). The results revealed that $Cs_2AgIn_{0.98}Bi_{0.02}Cl_6$ NCs and $Cs_2AgIn_{0.98}Bi_{0.02}Cl_6$@KIT-6 NCs suffered from fluorescence quenching at different levels with the increasing temperature, especially benefiting from the protection of the robust KIT-6 shell layer, and the loss of PL intensity in $Cs_2AgIn_{0.98}Bi_{0.02}Cl_6$@KIT-6 NCs was lower than that of $Cs_2AgIn_{0.98}Bi_{0.02}Cl_6$ NCs in high temperature environments. Moreover, the exciton binding energy (E_a) was often employed to estimate the thermal stability of inorganic crystalline materials, and the relationship between the PL intensity and the heating temperature of the samples was fitted by the Arrhenius equation,[21,41] so that the E_a values corresponding to $Cs_2AgIn_{0.98}Bi_{0.02}Cl_6$ NCs and $Cs_2AgIn_{0.98}Bi_{0.02}Cl_6$@KIT-6 NCs were obtained, respectively (Fig. 7b and f).

$$I(T) = \frac{I_0}{1 + A e^{-E_a/(kT)}} \quad (1)$$

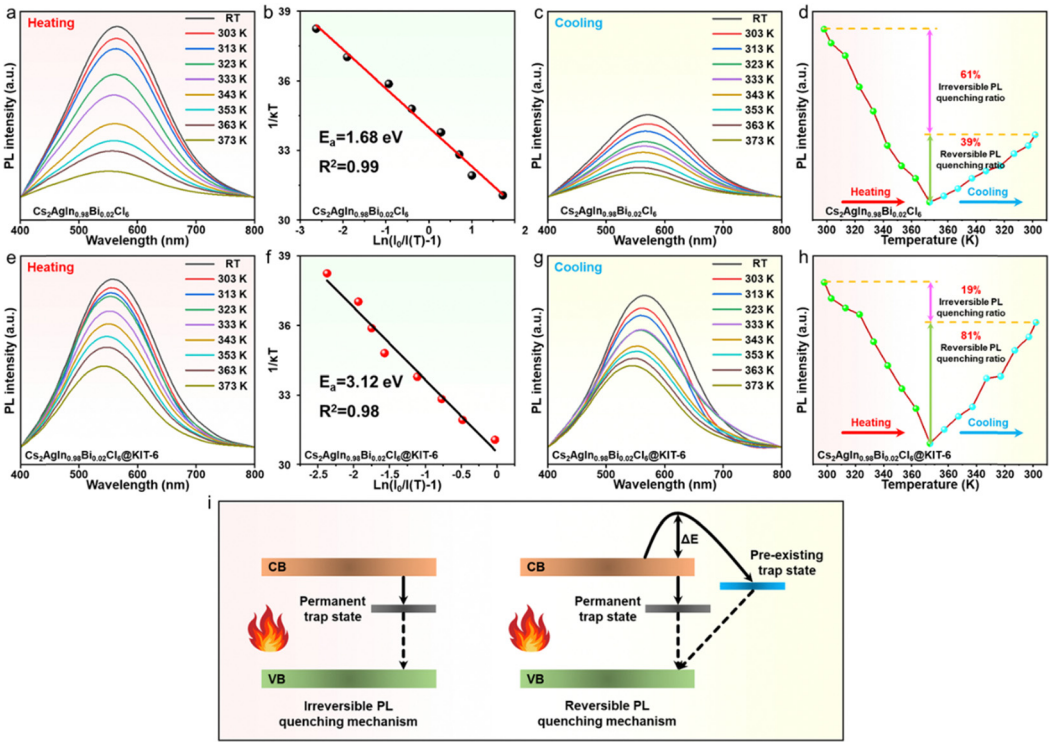

Fig. 7 PL spectra of $Cs_2AgIn_{0.98}Bi_{0.02}Cl_6$ NCs and $Cs_2AgIn_{0.98}Bi_{0.02}Cl_6$@KIT-6 NCs during heating (a) and (e) and cooling (c) and (g) cycles at 373 K, and their corresponding relationship between $\ln(I_0/I(T)-1)$ and $1/kT$ (b) and (f). Analysis of the relative changes in the PL intensity of $Cs_2AgIn_{0.98}Bi_{0.02}Cl_6$ NCs (d) and $Cs_2AgIn_{0.98}Bi_{0.02}Cl_6$@KIT-6 NCs (h) during heating–cooling cycles. (i) Schematic diagram of irreversible and reversible fluorescence quenching mechanisms.

where $I(T)$ is the PL intensity at different temperatures, I_0 is the initial PL intensity, A is a constant parameter, and k is the Boltzmann constant (8.629×10^{-5} eV K^{-1}). The fitting results indicated that KIT-6 on the surface of $Cs_2AgIn_{0.98}Bi_{0.02}Cl_6$@KIT-6 NCs can effectively be insulated from the external thermal environment, and its exciton binding energy was elevated to 3.12 eV under thermal disturbance, which was much higher than that of $Cs_2AgIn_{0.98}Bi_{0.02}Cl_6$ NCs (1.68 eV) without any protection. Afterwards, the PL spectra of the samples during the cooling process were recorded, and it can be seen that the PL spectra of both $Cs_2AgIn_{0.98}Bi_{0.02}Cl_6$ NCs and $Cs_2AgIn_{0.98}Bi_{0.02}Cl_6$@KIT-6 NCs gradually recovered as the ambient temperature was lowered; however, they could not be restored to their initial state (Fig. 7c and g). This phenomenon was mainly attributed to the emergence of two different trap states within the lead-free DP material in the thermal environment (Fig. 7i).[45] The recovery of PL intensity can be considered as a reversible fluorescence quenching, stemming from the thermally activated escape of carriers into existing (surface) trap states and/or the generation of thermally activated temporary trap states; these states relax during cooling, during which the fluorescence is recovered.[40] However, the PL intensity that cannot be recovered to the initial state can be assigned to irreversible fluorescence quenching, where changes in the crystal structure of the lead-free DP induced by the thermal environment contribute to the creation of irreversible permanent trap states, preventing the recovery of fluorescence.[41] Lastly, the variation of the PL intensity of $Cs_2AgIn_{0.98}Bi_{0.02}Cl_6$ NCs and $Cs_2AgIn_{0.98}Bi_{0.02}Cl_6$@KIT-6 NCs at different temperatures was registered statistically (Fig. 7d, h), and the PL quenching ratio of the samples under different quenching mechanisms was calculated using the following equations.[40,43]

$$\text{Irreversible PL quenching ratio} = \frac{I_i - I_r}{I_i - I_h} \quad (2)$$

$$\text{Reversible PL quenching ratio} = 1 - \text{irreversible PL quenching ratio} \quad (3)$$

where I_i is the PL intensity at the initial room temperature, I_r is the PL intensity recovered to room temperature after cycling, and I_h is the PL intensity heated to the highest temperature (373 K). The calculation results indicated an irreversible PL quenching ratio of 61% for $Cs_2AgIn_{0.98}Bi_{0.02}Cl_6$ NCs without any coating protection (Fig. 7d), which suggested that only 39% of the initial fluorescence for $Cs_2AgIn_{0.98}Bi_{0.02}Cl_6$ NCs was retained after undergoing a high-temperature cooling cycle, greatly detrimental to its subsequent further application in optical devices. In contrast, the irreversible quenching ratio of $Cs_2AgIn_{0.98}Bi_{0.02}Cl_6$@KIT-6 NCs was reduced to 19% (Fig. 7h), and the enhanced thermal stability was attributed to the fact that the robust KIT-6 mesoporous molecular sieves on the surface effectively prevented the heat transmission

between the external heat source and B, making it more suitable for optoelectronic lighting applications.

For the simulation of the working stability between $Cs_2AgIn_{0.98}Bi_{0.02}Cl_6$ NCs and $Cs_2AgIn_{0.98}Bi_{0.02}Cl_6$@KIT-6 NCs under actual optoelectronic device application, they were assembled with UV chips as two LEDs, respectively, but the surface of the optoelectronic device inevitably warmed up during long-time energized operation, which was fatal to the optical emission of $Cs_2AgIn_{0.98}Bi_{0.02}Cl_6$ NCs and $Cs_2AgIn_{0.98}Bi_{0.02}Cl_6$@KIT-6 NCs. Here, a thermal infrared imager was utilized to record the temperature variations on the surface of the LED device in real time, thus providing insight into the functional relationship between the energization time and the surface temperature of the device. Additionally, variations in the spectra and associated optoelectronic parameters of the two LEDs were monitored by using a highly sensitive spectrometer, so that the device performance could be further evaluated (Fig. 8a). The electroluminescence intensity of the $Cs_2AgIn_{0.98}Bi_{0.02}Cl_6$ NC and $Cs_2AgIn_{0.98}Bi_{0.02}Cl_6$@KIT-6 NC assembled LED devices was gradually enhanced with the driving current, and no noticeable apparent saturation phenomenon was found (Fig. 8c, f), which implies that they are more suitable for subsequent development in high-power commercial lighting systems. Correspondingly, the correlated color temperature (CCT) of the two LEDs was also boosted, the CCT values of the devices assembled by $Cs_2AgIn_{0.98}Bi_{0.02}Cl_6$ NCs and $Cs_2AgIn_{0.98}Bi_{0.02}Cl_6$@KIT-6 NCs reached 2829 K and 2972 K, and the color rendering indexes (CRIs) were 81 and 86, respectively, when the driving current was 100 mA (Fig. S10a, c). Under power-on conditions, the LED devices assembled with $Cs_2AgIn_{0.98}Bi_{0.02}Cl_6$ NCs and $Cs_2AgIn_{0.98}Bi_{0.02}Cl_6$@KIT-6 NCs both emitted bright yellow lights (insets of Fig. S10b and d, ESI†), corresponding to the color coordinates in the International Commission on Illumination (CIE) charts as (0.46, 0.45) and (0.46, 0.46) respectively, belonging to the standard yellow light region (Fig. S10b and d, ESI†). Subsequently, the thermal infrared imager recorded the surface temperatures of the LED devices assembled with $Cs_2AgIn_{0.98}Bi_{0.02}Cl_6$ NCs and $Cs_2AgIn_{0.98}Bi_{0.02}Cl_6$@KIT-6 NCs during high power (100 mA) operation as a function for the operating time (Fig. 8b). Unsurprisingly, the surface temperature of the LED devices gradually increased with the prolongation of the energization time, and the surface temperature of the devices reached 326.8 K after 270 min of continuous working. At the same time, the EL intensities of the two LEDs showed different degrees of degradation with power-on time (Fig. 8d, g), which was

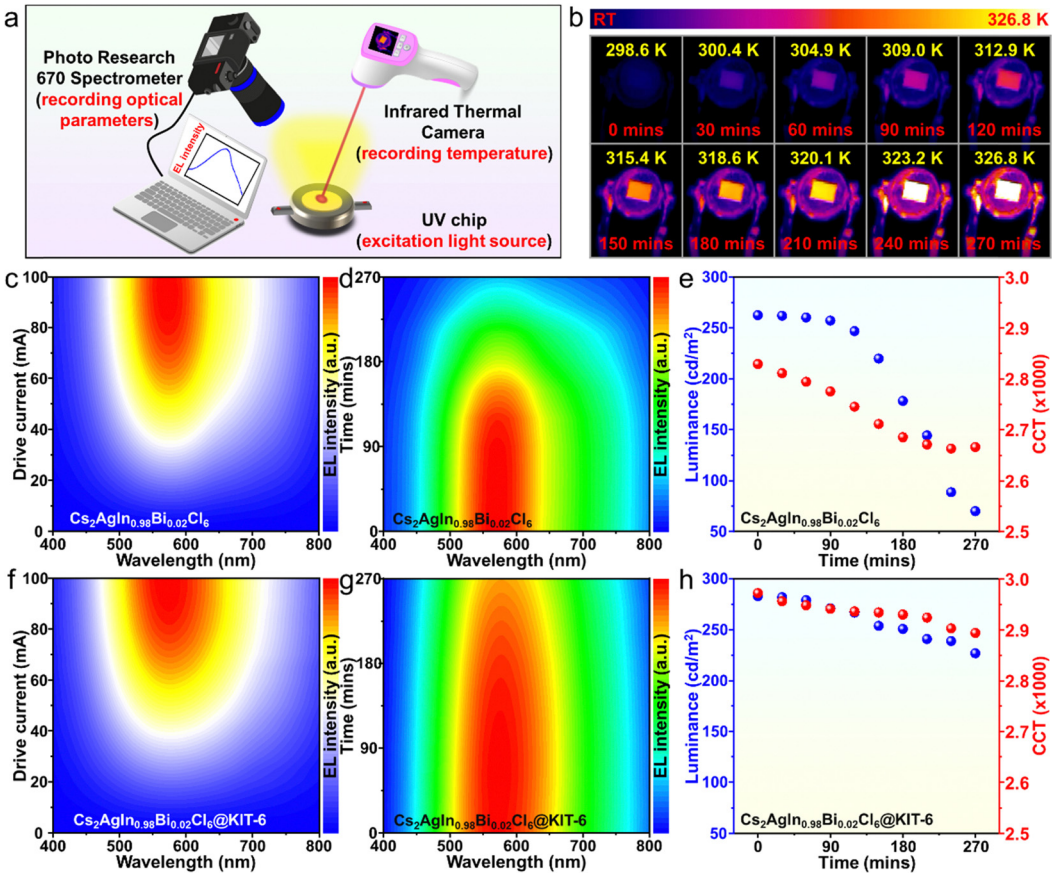

Fig. 8 (a) Schematic of the surface temperature and EL spectra of LED devices recorded at different operating times. (b) Infrared images and surface temperature of LED devices driven by a 100 mA current with extended working time. (c) and (f) EL spectra of the devices assembled using $Cs_2AgIn_{0.98}Bi_{0.02}Cl_6$ NCs and $Cs_2AgIn_{0.98}Bi_{0.02}Cl_6$@KIT-6 NCs with increased driving current. (d) and (g) EL spectra changes of two LED devices operating at 100 mA for 270 min, and their corresponding (e) and (h) luminous efficacy (blue dot) and CCT values (red dot).

inextricably linked to the elevated surface temperature of the devices. It can be observed from the corresponding optoelectronic parameters of the LED devices that the luminous efficiency and CCT values of the LED devices do not float drastically during the initial 90 minutes (Fig. 8e and h), the surface temperature of the devices was not higher at this time, and the impact on the optical performance of $Cs_2AgIn_{0.98}Bi_{0.02}Cl_6$ NCs and $Cs_2AgIn_{0.98}Bi_{0.02}Cl_6$@KIT-6 NCs was relatively weaker. As the working time was further extended, the photoelectric parameters of the LED devices assembled with $Cs_2AgIn_{0.98}Bi_{0.02}Cl_6$@KIT-6 NCs changed drastically, and after 270 min of continuous operation, the luminous efficiency decreased from the initial 262.6 cd m^{-2} to 69.8 cd m^{-2}, and the CCT value also sharply decayed to 2664 K (Fig. 8e). In contrast, benefiting from the robust KIT-6 protection, the LED assembled with $Cs_2AgIn_{0.98}Bi_{0.02}Cl_6$@KIT-6 NCs maintained 80% of its initial luminous efficiency (283.6 cd m^{-2}) after operating for 270 min (227.2 cd m^{-2}), and the corresponding CCT values did not fluctuate much (from 2972 K to 2894 K) (Fig. 8h), indicating that $Cs_2AgIn_{0.98}Bi_{0.02}Cl_6$@KIT-6 NCs were more suitable for the development of stable high-power illumination devices. In conclusion, the $Cs_2AgIn_{0.98}Bi_{0.02}Cl_6$@KIT-6 NCs obtained by the *in situ* assembly method exhibited excellent performance in practical display device applications. The stable KIT-6 shell layer on their surface can effectively protect $Cs_2AgIn_{0.98}Bi_{0.02}Cl_6$ NCs, so that the fluorescence intensity degradation can be alleviated under long-time energization conditions, which greatly enhanced the competitiveness of the lead-free DP NCs in the future optoelectronic market.

Conclusions

In summary, $Cs_2AgIn_xBi_{1-x}Cl_6$ NCs were successfully synthesized within the pores of KIT-6 mesoporous molecular sieves using an *in situ* assembly method. The fine-tuning of the In/Bi ratio led to the formation of $Cs_2AgIn_{0.98}Bi_{0.02}Cl_6$@KIT-6 NCs, characterized by their superior optical properties. Thermal stability assessments indicated that these core–shell NCs demonstrate enhanced fluorescence stability during high-temperature thermal cycling, in contrast to pure $Cs_2AgIn_{0.98}Bi_{0.02}Cl_6$ NCs. This improvement is attributed to the reduction in internal permanent defect states post-heating. Subsequently, the orange LED assembled using $Cs_2AgIn_{0.98}Bi_{0.02}Cl_6$@KIT-6 NCs maintained 80% of its initial luminous efficiency after 270 min of operation at high power, while $Cs_2AgIn_{0.98}Bi_{0.02}Cl_6$ NCs sharply decreased to 26%, and the infrared camera recorded that the surface temperature of the device reached 326.8 K at this time. These findings underscore the efficacy of the *in situ* assembly process in enhancing the optical stability of lead-free DP materials. This advancement is a crucial step toward the development of highly stable, lead-free LED devices, paving the way for broader applications of lead-free DP materials in optoelectronic screen displays.

Author contributions

Jindou Shi: conceptualization (lead), investigation (lead), methodology (lead), and writing – original draft preparation (lead); Zeyu Wang: conceptualization (equal) and writing – review and editing (lead); Luxia Xu: conceptualization (equal); Junnan Wang: conceptualization (equal); Zheyuan Da: investigation (equal); Chen Zhang: investigation (equal); Yongqiang Ji: investigation (equal); Qing Yao: investigation (equal); Youlong Xu: investigation (equal); Nikolai V. Gaponenko: investigation (equal); Jinshou Tian: conceptualization (equal); Minqiang Wang: conceptualization (equal), funding acquisition (lead), and writing – review and editing (lead).

Conflicts of interest

There are no conflicts to declare.

Acknowledgements

This work was supported by the National Key R&D Program of China (2022YFE0122500 and 2019YFB1503200), the National Natural Science Foundation of China (NSFC, 52161145103 and 61774124), the 111 Program (No. B14040), and the Shaanxi Provincial Key Research and Development Program (No. 2021GXLH-Z-084). The authors thank Ms Dan He at the Instrument Analysis Center of Xi'an Jiaotong University for her help with the time-resolved PL analysis.

Notes and references

1 L. Zhou, Y. F. Xu, B. X. Chen, D. B. Kuang and C. Y. Su, *Small*, 2018, **14**, 1703762.
2 H. W. Lei, D. Hardy and F. Gao, *Adv. Funct. Mater.*, 2021, **31**, 2105898.
3 Z. X. Li, P. Wang, C. Ma, F. Igbari, Y. K. Kang, K. L. Wang, W. Y. Song, C. Dong, Y. J. Li, J. S. Yao, D. Meng, Z. K. Wang and Y. Yang, *J. Am. Chem. Soc.*, 2021, **143**, 2593–2600.
4 Z. H. Shuang, H. Zhou, D. J. Wu, X. H. Zhang, B. Xiao, G. K. Ma, J. Zhang and H. Wang, *Chem. Eng. J.*, 2022, **433**, 134544.
5 T. Y. Wang, H. L. Loi, J. P. Cao, Z. T. Qin, Z. Q. Guan, Y. Xu, H. Y. Cheng, M. G. Li, C. S. Lee, X. H. Lu and F. Yan, *Adv. Sci.*, 2022, **9**, 2200242.
6 J. D. Shi, Z. Y. Wang, N. V. Gaponenko, Z. Da, C. Zhang, J. N. Wang, Y. Q. Ji, Y. S. Ding, Q. Yao, Y. L. Xu and M. Q. Wang, *Small*, 2024, 2310478.
7 J. N. Li, X. H. Meng, Z. H. Wu, Y. Y. Duan, R. X. Guo, W. D. Xiao, Y. S. Zhang, Y. K. Li, Y. L. Shen, W. Zhang and G. S. Shao, *Adv. Funct. Mater.*, 2022, **32**, 2112991.
8 N. Ding, L. Shao, T. Y. Xie, G. C. Pan, D. L. Zhou, X. Bai, S. Y. Lu, J. H. Hu, J. Zhou, W. Xu and H. W. Song, *Laser Photonics Rev.*, 2022, **16**, 2200301.
9 Z. Y. Zhang, Q. D. Sun, Y. Lu, F. Lu, X. L. Mu, S. H. Wei and M. L. Sui, *Nat. Commun.*, 2022, **13**, 3397.

10 Y. Z. He, Y. F. Zhou, Q. Wang, Q. X. Hao, X. W. Guo and S. R. Li, *Sol. RRL*, 2023, **7**, 2300030.
11 H. Li, C. J. Pi, W. Q. Chen, M. Zhou, J. M. Wei, J. H. Yi, P. Song, Y. Alexey, Y. Zhong, X. Yu, J. B. Qiu and X. H. Xu, *J. Phys. Chem. Lett.*, 2021, **12**, 5682–5688.
12 J. D. Shi, Z. Y. Wang, N. Gaponenko, Z. Da, C. Zhang, J. N. Wang, Y. Q. Ji, Q. Yao, Y. S. Ding, M. Q. Wang and Y. L. Xu, *Mater. Today Chem.*, 2024, **3**, 101874.
13 X. W. Cheng, Z. Xie, W. Zheng, R. F. Li, Z. H. Deng, D. T. Tu, X. Y. Shang, J. Xu, Z. L. Gong, X. J. Li and X. Y. Chen, *Adv. Sci.*, 2022, **9**, 2103724.
14 B. Zhou, Z. X. Liu, S. F. Fang, H. Z. Zhong, B. B. Tian, Y. Wang, H. N. Li, H. L. Hu and Y. M. Shi, *ACS Energy Lett.*, 2021, **6**, 3343–3351.
15 J. Y. Sun, W. Zheng, P. Huang, M. R. Zhang, W. Zhang, Z. H. Deng, S. H. Yu, M. Y. Jin and X. Y. Chen, *Angew. Chem., Int. Ed.*, 2022, **61**, e202201993.
16 J. D. Shi, M. Q. Wang, C. Zhang, J. N. Wang, Y. Zhou, Y. L. Xu, N. V. Gaponenko and A. S. Bhatti, *ACS Appl. Mater. Interfaces*, 2023, **15**, 12383–12392.
17 J. D. Shi, M. Q. Wang, C. Zhang, J. N. Wang, Y. Zhou, Y. L. Xu and N. V. Gaponenko, *J. Mater. Chem. C*, 2023, **11**, 4742–4752.
18 J. D. Shi, M. Q. Wang, C. Zhang, J. N. Wang, Y. Zhou, Y. L. Xu and N. V. Gaponenko, *Mater. Today Chem.*, 2023, **29**, 101480.
19 F. Locardi, E. Sartori, J. Buha, J. Zito, M. Prato, V. Pinchetti, M. L. Zaffalon, M. Ferretti, S. Brovelli, I. Infante, L. De Trizio and L. Manna, *ACS Energy Lett.*, 2019, **4**, 1976–1982.
20 J. H. Ji, G. Jo, J. G. Ha, S. M. Koo, M. Kamiko, J. Hong and J. H. Koh, *J. Nanosci. Nanotechnol.*, 2018, **18**, 6029–6032.
21 M. M. Liu, Q. Wan, H. M. Wang, F. Carulli, X. C. Sun, W. L. Zheng, L. Kong, Q. Zhang, C. Y. Zhang, Q. G. Zhang, S. Brovelli and L. Li, *Nat. Photonics*, 2021, **15**, 379.
22 X. Y. Lu, T. C. Hua and Y. P. Wang, *Microelectron. J.*, 2011, **42**, 1257–1262.
23 Y. Y. Tang, M. L. Liang, B. D. Chang, H. Y. Sun, K. B. Zheng, T. Pullerits and Q. J. Chi, *J. Mater. Chem. C*, 2019, **7**, 3369–3374.
24 T. Zuo, F. F. Qi, C. Yam and L. Y. Meng, *Phys. Chem. Chem. Phys.*, 2022, **24**, 26948–26961.
25 A. Pasha, S. Akhil and R. G. Balakrishna, *J. Mater. Chem. A*, 2021, **9**, 17701–17719.
26 J. Zhou, Z. G. Xia, M. S. Molokeev, X. W. Zhang, D. S. Peng and Q. L. Liu, *J. Mater. Chem. A*, 2017, **5**, 15031–15037.
27 S. Li, Z. F. Shi, F. Zhang, L. T. Wang, Z. Z. Ma, D. Wu, D. W. Yang, X. Chen, Y. T. Tian, Y. T. Zhang, C. X. Shan and X. J. Li, *ACS Appl. Mater. Interfaces*, 2020, **12**, 46330–46339.
28 A. Karmakar, M. S. Dodd, S. Agnihotri, E. Ravera and V. K. Michaelis, *Chem. Mater.*, 2018, **30**, 8280–8290.
29 N. Chen, T. Cai, W. H. Li, K. Hills-Kimball, H. J. Yang, M. D. Que, Y. Nagaoka, Z. Y. Liu, D. Yang, A. G. Dong, C. Y. Xu, R. Zia and O. Chen, *ACS Appl. Mater. Interfaces*, 2019, **11**, 16855–16863.
30 D. X. Zhu, J. Zito, V. Pinchetti, Z. Y. Dang, A. Olivati, L. Pasquale, A. W. Tang, M. L. Zaffalon, F. Meinardi, I. Infante, L. De Trizio, L. Manna and S. Brovelli, *ACS Energy Lett.*, 2020, **5**, 1840–1847.
31 M. Fan, J. P. Huang, L. Turyanska, Z. F. Bian, L. C. Wang, C. Y. Xu, N. Liu, H. B. Li, X. Y. Zhang, C. X. Zhang and X. Y. Yang, *Adv. Funct. Mater.*, 2023, **33**, 2215032.
32 J. Y. Sun, F. T. Rabouw, X. F. Yang, X. Y. Huang, X. P. Jing, S. Ye and Q. Y. Zhang, *Adv. Funct. Mater.*, 2017, **27**, 1704371.
33 H. L. Xu, H. Yang, G. T. Xu and Y. X. Yang, *MATEC Web Conf.*, 2016, **67**, 01006.
34 J. D. Majher, M. B. Gray, T. A. Strom and P. M. Woodward, *Chem. Mater.*, 2019, **31**, 1738–1744.
35 W. W. Meng, X. M. Wang, Z. W. Xiao, J. B. Wang, D. B. Mitzi and Y. F. Yan, *J. Phys. Chem. Lett.*, 2017, **8**, 2999–3007.
36 B. Yang, X. Mao, F. Hong, W. W. Meng, Y. X. Tang, X. S. Xia, S. Q. Yang, W. Q. Deng and K. L. Han, *J. Am. Chem. Soc.*, 2018, **140**, 17001–17006.
37 G. Y. Zhang, D. Y. Wang, B. B. Lou, C. G. Ma, A. Meijerink and Y. H. Wang, *Angew. Chem., Int. Ed.*, 2022, **61**, e202207454.
38 P. Han, X. Mao, S. Yang, F. Zhang, B. Yang, D. Wei, W. Deng and K. Han, *Angew. Chem., Int. Ed.*, 2019, **58**, 17231–17235.
39 B. A. Connor, L. Leppert, M. D. Smith, J. B. Neaton and H. I. Karunadasa, *J. Am. Chem. Soc.*, 2018, **140**, 5235–5240.
40 J. D. Shi, M. Q. Wang, Z. Da, C. Zhang, J. N. Wang, Y. S. Ding, Y. L. Xu and N. V. Gaponenko, *Nanoscale*, 2023, **15**, 11190–11198.
41 J. D. Shi, W. Y. Ge, Y. Tian, M. M. Xu, W. X. Gao and Y. T. Wu, *Small*, 2021, **17**, 2006568.
42 J. D. Shi, W. Y. Ge, J. F. Zhu, M. Saruyama and T. Teranishi, *ACS Appl. Nano Mater.*, 2020, **3**, 7563–7571.
43 J. D. Shi, M. Q. Wang, H. Wang, C. Zhang, Y. Q. Ji, J. N. Wang, Y. Zhou and A. S. Bhatti, *Nanoscale*, 2022, **14**, 16548–16559.
44 M. M. Zhu, Y. P. Liu, H. J. Ding, S. L. Zhang, M. J. Qu, T. T. Xuan and H. L. Li, *J. Am. Ceram. Soc.*, 2023, **106**, 7503–7513.
45 Y. M. Zhao, C. Riemersma, F. Pietra, R. Koole, C. D. Donega and A. Meijerink, *ACS Nano*, 2012, **6**, 9058–9067.